Nonlinear elasticity of biological basement membrane revealed by rapid inflation and deflation

Hui Li[a,b,1,2], Yue Zheng[c,1], Yu Long Han[b], Shengqiang Cai[c,2], and Ming Guo[b,2]

[a]School of Systems Science, Beijing Normal University, Beijing 100875, China; [b]Department of Mechanical Engineering, Massachusetts Institute of Technology, Cambridge, MA 02139; and [c]Department of Mechanical and Aerospace Engineering, University of California San Diego, La Jolla, CA 92093

Basement membrane (BM) is a thin layer of extracellular matrix that surrounds most animal tissues, serving as a physical barrier while allowing nutrient exchange. Although they have important roles in tissue structural integrity, physical properties of BMs remain largely uncharacterized, which limits our understanding of their mechanical functions. Here, we perform pressure-controlled inflation and deflation to directly measure the nonlinear mechanics of BMs in situ. We show that the BMs behave as a permeable, hyperelastic material whose mechanical properties and permeability can be measured in a model-independent manner. Furthermore, we find that BMs exhibit a remarkable nonlinear stiffening behavior, in contrast to the reconstituted Matrigel. This nonlinear stiffening behavior helps the BMs to avoid the snap-through instability (or structural softening) widely observed during the inflation of most elastomeric balloons and thus maintain sufficient confining stress to the enclosed tissues during their growth.

basement membrane | nonlinear mechanics | strain stiffening | extracellular matrix | permeability

Basement membrane (BM) is a thin layer of fibrous matrix separating cells from the connecting tissues, which functions as a physical barrier and widely exists across multicellular organisms (1). The BM is typically composed of laminins, collagen IV, nidogens, and proteoglycans; laminin and collagen IV are the major components that constitute networks forming the structure of the BM, and nidogen and proteoglycans are associated with the laminin and collagen IV networks. As a physical barrier, the structural and mechanical properties of BM are important in the organization and morphogenesis of tissues and organs as well as in the maintenance of adult functions (2); abnormal BM has been associated with a variety of diseases such as cancer (3). For example, in metastasis, cancer cells must invade through BMs to escape from the primary tumor—a process that causes 90% of cancer-related death (4). Indeed, breaks in BMs can be observed in malignant tumors (5). Thus, mechanical properties of the BM are considered to play important roles in regulating cancer cell invasion (6, 7). Furthermore, as a physical barrier differentiating different parts of tissues, BMs are required to be permeable to small molecules to allow exchange of water and nutrients; the permeability of BM is thus one of the essential kinetic parameters regulating biomolecule exchange and activities of internal cells (8, 9). Given the importance of BMs as a semipermeable barrier maintaining tissue structural integrity, however, their permeability and mechanical properties remain largely unknown, mainly due to the lack of direct measurement methods, especially in situ. This limits our understanding of the physical role of BMs in various physiological and pathological processes such as tumor development and angiogenesis.

Determining the mechanical properties of intact BMs in situ is challenging because of their irregular shape, small thickness, and tight connection to the cells inside. Due to these limitations, conventional mechanical tests such as tensile, compression, and bending tests are difficult to be applied to characterize the mechanical behavior of the BM in situ. Instead, previous measurements had been carried out on fragmented BMs isolated from various tissues (e.g., via atomic force microscopy [AFM] indentation) and found that the BM stiffness ranges from ∼kPa to ∼MPa (10–17). In addition, a constitutive relationship is required to extract the material parameters such as elastic modulus and permeability from these experimental measurements. However, like most biological tissues, a reliable constitutive model for the BM is not yet available, causing additional difficulties in obtaining its mechanical parameters from most traditional experiments.

In this work, we demonstrate an in situ method to simultaneously measure both the elastic properties and permeability of intact BM in breast cancer spheroid by recording the deflation process of an inflated BM filled with phosphate buffered saline (PBS) by microinjection without requiring complex sample preparation and post-data processing. During the deflation of the BM, its elastic retraction generates a pressure difference to drive the liquid flow through the membrane; the liquid flux can be calculated from the reduction of the intact BM diameter. With the BM thickness measured by transmission electron microscopy (TEM), we can determine the shear modulus, permeability, and diffusivity of the intact BM. Moreover, we find from our measurements that the elasticity of BM is highly nonlinear with a strong strain-stiffening effect. Furthermore, we discuss the possible impact of the strain-stiffening effects of BM on its functions.

Significance

Basement membranes (BMs) are thin layers of extracellular matrix ubiquitously found in animals surrounding various tissues. As a physical barrier, their mechanical properties are important in maintaining structural integrity of tissues, and their permeabilities are essential for molecule exchange and internal cell activities. However, due to the lack of direct measurement methods, the physical properties of BMs remain largely unclear, limiting our understanding of BMs in various physiological and pathological processes such as tumor development. Here, we apply pressure-controlled inflation/deflation to measure the stress–strain behaviors of intact BM in situ and to determine the mechanical properties in a model-independent manner. We discover a strong strain-stiffening effect of intact BM, which is essential for preventing its snap-through instability.

BIOPHYSICS AND COMPUTATIONAL BIOLOGY

Results

To investigate the mechanics of BM, we fabricate three-dimensional breast cancer spheroids (18, 19). Briefly, individual human breast cancer MDA-MB-231 cells are seeded onto a gelled Matrigel bed (10 mg/mL) and are cultured to allow proliferation for 5 d to form clusters. BM is secreted and generated by cells during the growth of these multicellular cancer spheroids. After that, the intact cancer spheroids with BM are isolated from the Matrigel and seeded on a glass-bottom Petri dish for subsequent microinjection. The BM remains intact on these cancer spheroids (Fig. 1 *A* and *C*).

To examine the structure of the BM of these cancer spheroids, we first perform immunofluorescent imaging of the BM in extracted spheroids by labeling laminin-5, one of the major components of BM (Fig. 1*C*). Indeed, we see a continuous layer of laminin-5 surrounding the cancer spheroid, suggesting that the BM is nicely formed on these spheroids. To further investigate the structure and thickness of these BMs, we perform TEM imaging on in situ BM sections, which could preserve the original condition of the BM. To do so, cancer cell spheroids that partly embed in Matrigel are fixed on day 5, then sectioned and stained according to established protocols (20). The cross-sections of the spheroid above the Matrigel surface are collected and used for TEM imaging. It is apparent that a gray layer of BM surrounds the cell clusters inside (Fig. 1*A*). As we zoom in, clear fibrous structures of the BM can be observed (Fig. 1*B*). From these images, we find that the thickness of BM in our cancer spheroid system is 2.5 ± 1.2 μm (Fig. 1*D*). Interestingly, the thickness of BMs has obvious variations, even on the same spheroid. This is likely to be a result of cell-to-cell variation as the BM is locally generated by adjacent cells.
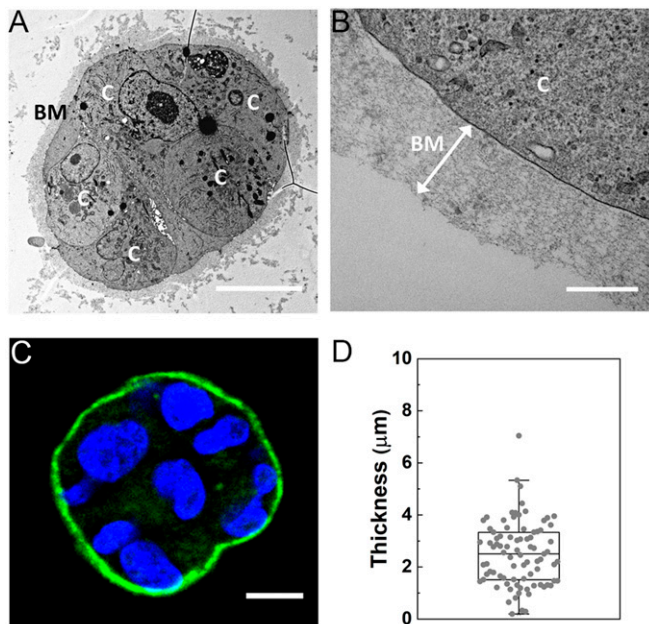
To study the mechanics of BM, we perform an inflation and deflation experiment of the BM surrounding the spheroid in situ. To do so, we use a microneedle (2 μm in diameter) to penetrate the surrounding BM and place the needle tip inside the spheroid. We then apply a constant pressure to inject PBS solution into the spheroid via the microneedle. Both the injection pressure and its duration are precisely controlled by a microinjector that connects to the microneedle (Fig. 2*A*). Interestingly, upon a constant pressure, we observe that the BM detaches from the inside cell aggregations and inflates into a spherical shape like a latex balloon; it rapidly inflates to a steady state (Fig. 2*B*), at which the continuous PBS influx is balanced by the outflow through the semipermeable membrane. When the fluid influx is turned off, the inflated BM gradually deflates back to its initial size as a result of the elasticity of the membrane, which drives the outflow of liquid through the semipermeable BM. We find this inflation and deflation process is highly reversible, suggesting that the BM is deformed elastically during this process. Typically, to fully separate the BM from the cell cluster, we perform several rounds of inflation/deflation prior to final experiments. The spherical shape of an inflated BM suggests that the BM is fully isolated from cells (Fig. 2*B*); thus, its shape is dominated by the balance of membrane tension and cross-membrane pressure difference.

To quantitatively investigate the inflation and deflation process, we perform continuous imaging at 14 Hz via bright-field microscopy to record the shape and size of a BM during this process (Fig. 2*C* and [Movie S1](#)). This allows us to measure the radius of the BM and its change over time, as shown by the kymograph in Fig. 2*C* and quantification in Fig. 2*D*. The quantitative inflation and deflation curves indeed remain the same over different loading cycles, demonstrating good resilience of BM. Although the inflation process is rapid, especially under large injection pressure, the deflation process is relatively slow, as shown by the rapid increase and gradual decrease of BM radius (Fig. 2*D*). Furthermore, we repeat this experiment using different injection pressures; as the injection pressure is increased, the radius of the inflated BM at steady state is increased accordingly (Fig. 2*D* and *SI Appendix*, [Fig. S1](#)).

To understand the steady-state inflation as well as the deflation process of a BM, we consider a spherical membrane with inner radius R_0 and membrane thickness H prior to deformation while no pressure is applied. With the inner fluid pressure p, the inner radius increases to r, and wall thickness reduces to h. For simplicity, in the following analysis, we assume the fluid pressure is homogenous and neglect the inertial effect of the membrane during the deflation because the process is relatively slow.

For an inflated spherical membrane, any point in the membrane is in an equal-biaxial stress (and stretch) state. We denote the equal-biaxial hoop stretch as λ and the stress as σ. Simple geometrical analysis shows that the biaxial hoop stretch equals the radial expansion, namely $\lambda = r/R_0$. With different levels of the inflation pressure p, the corresponding maximal stretches in the steady state $\lambda_{max} = r_{max}/R_0$ of the membrane before the deflation begins are plotted in Fig. 3*A*. During the deflation processes, the decreases of the radial expansion with time for five different inflation pressures are shown in Fig. 3*B*. The water flux J is related to the radius of the BM as $J = -dr/dt$ with the assumption of the incompressibility of water, thus the flux can be plotted as a function of stretch for different experiments, as $J = J(\lambda)$ shown in Fig. 3*C*. Notably, the relationships between J and λ obtained under different injection pressures on the same BM overlap.

Next, we will show that the constitutive behavior of the membrane can be directly deduced from the results shown in Fig. 3 *A* and *C*. We assume the constitutive behavior of the membrane subject to equal-biaxial stress (σ) is given by $\sigma = \sigma(\lambda)$. The force balance requires $\sigma = pr/2h$. With the commonly adopted assumption for soft tissues that the membrane material

Fig. 1. TEM and fluorescence images of BMs in cancer spheroids. (*A*) In situ TEM images of a cell spheroid partly embedded in Matrigel matrix. The top cross-sections of the spheroid above the Matrigel surface are collected and imaged. The gray layer surrounding the aggregated cells (marked as C) is the BM. (Scale bar, 10 μm.) (*B*) A magnified image of the BM shows the fiber-like structure. (Scale bar, 500 nm.) (*C*) Immunofluorescence images of laminin-5 in the BM (green) from an extracted cell spheroid. The cell nuclei are labeled by Hoechst 33342 (blue). (Scale bar, 10 μm.) (*D*) The thickness of BMs measured from TEM images, with an average value 2.5 ± 1.2 μm. *n* = 85 measurements from 11 spheroids.
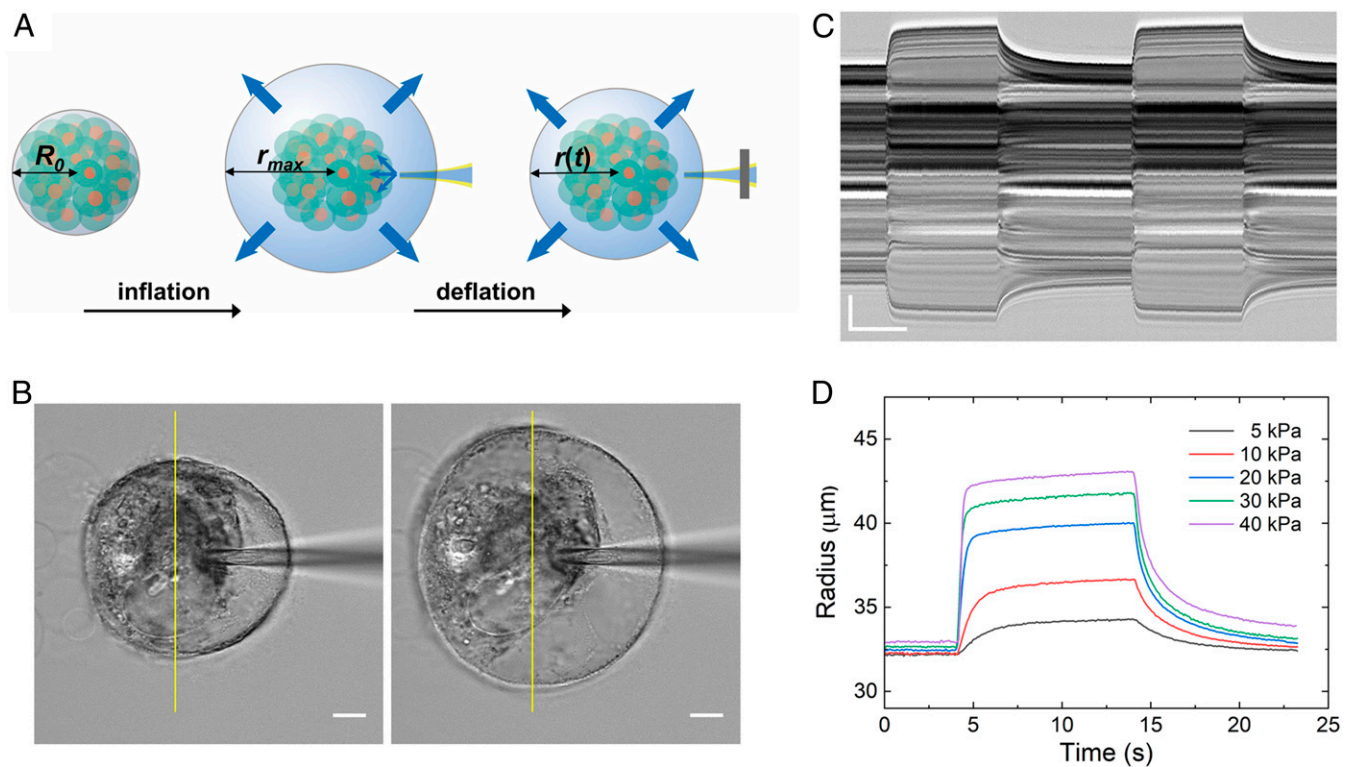
Fig. 2. Experimental setup. (*A*) A schematic of the experimental setup. (*B*) Spherical BM before (*Left*) and under the injection at 20 kPa (*Middle*). (Scale bar, 10 μm.) The inside cell spheroid is predetached from the surrounding BM by several injections. (*C*) Kymograph of two inflation and deflation processes of the BM under an injection pressure 20 kPa. (Scale bars, vertically 10 μm and horizontally 5 s.) (*D*) The measured radius of BM during inflations and deflations under increased injection pressures.

is incompressible, the thickness of the membrane after inflation can be related to the stretch as $h = H\lambda^{-2}$. Consequently, the relationship between biaxial membrane stress and internal fluid pressure becomes $\sigma(\lambda) = \frac{R_0}{2H}\lambda^3 p(\lambda)$. Without requiring any material model or assumption, using measured function $p(\lambda)$ as shown in Fig. 3*A*, the constitutive function $\sigma(\lambda)$ can be fully determined with up to one constant $\frac{R_0}{2H}$. Both R_0 and H can be easily obtained from bright-field or TEM imaging. With measured $R_0 = 32.5\mu m$ and $H = 2.5\mu m$, we obtain biaxial stress–stretch relationship $\sigma(\lambda)$ of BM from inflation–deflation tests, as shown by black circles in Fig. 3*D*.

We next compare the above experimentally determined constitutive relationship with existing hyperelastic models. Based on the shape of the function $\sigma = \sigma(\lambda)$ shown in Fig. 3*D*, we choose Fung's hyperelastic model as an example. It can be shown that with strain energy function proposed by Fung (21): $W = \frac{G}{2b}(e^{b(\lambda_1^2+\lambda_2^2+\lambda_3^2-3)} - 1)$, the relationship between the equal-biaxial stress and stretch is given by the following equation:

$$\sigma = G\left(\lambda^2 - \frac{1}{\lambda^4}\right)e^{b\left(2\lambda^2 + \frac{1}{\lambda^4} - 3\right)}, \qquad [1]$$

where G and b are two material constants. G can be regarded as shear modulus of the material and b is a dimensionless parameter related to the strain stiffening of the material. By fitting the prediction from Eq. **1** to the experimental data in Fig. 3*D*, we obtain these material constants for this particular BM, as $G = 82.30$ kPa and $b = 2.10$. The measured G is consistent with previous measurements on isolated BMs, for example, the elastic modulus of corneal BM (80 kPa, which is roughly three times of the shear modulus for an incompressible solid) (11) and BM from *Drosophila* eggs (70 kPa) (12). Moreover, we compare

the predictions of different hyperelastic models with our experimental measurements, in addition to Fung's model. We find that Fung's model gives a better description to the experimental stress–strain relationship of BMs as compared to several other models such as neo-Hookean, Mooney–Rivlin model, or the Gent model (*SI Appendix*, Fig. S2).

To understand the kinetic properties of the BM, we adopt Darcy's law to determine the water flux J passing through the membrane as $J = \frac{k}{\mu}\frac{p}{h}$, where k is diffusivity of the membrane while μ is dynamic viscosity of the fluid. The equations above enable us to further obtain that $\sigma = \frac{\mu R_0}{2k}\lambda J$. So with knowing the number $\frac{\mu}{2k}$, we can also obtain the constitutive function $\sigma = \sigma(\lambda)$ from $J = J(\lambda)$ shown in Fig. 3*C*. By choosing $\frac{\mu}{2k}$ to be 0.72 kPa · s/μm², the constitutive relation determined from Fig. 3*C* agrees extremely well with the constitutive relation shown in Fig. 3*D*. Finally, with the dynamic viscosity of the aqueous solution as $\mu = 1mpa \cdot s$, we can estimate the permeability of the BM $k = 6.95 \times 10^{-19}$ m². This is consistent with previous measurement on isolated lens BMs from bovine eye (22). Furthermore, if we adopt the diffusivity as $D = kG/\mu$, we can obtain the poroelastic diffusion coefficient $D = 5.72 \times 10^{-11}$ m²/s.

By comparing in situ inflation and deflation curves in experiments to analytical solution, we can obtain several key materials parameters of the BM, as summarized in *SI Appendix*, Table S1. We indeed observe a significant variation of the measured values. These variations reflect structural and mechanical differences among these BMs as they are locally produced by each cancer cell spheroid and thus may vary both BM thickness and membrane structures (11, 23).

The inflation–deflation process reveals the nonlinear elastic behavior of the BM. From the measured biaxial stress–strain diagram of BMs shown in Fig. 3 *A* and *D*, we observe significant nonlinearity and strain-stiffening effects. Based on Fung's model,

Li et al.
Nonlinear elasticity of biological basement membrane revealed by rapid inflation and deflation

PNAS | 3 of 6
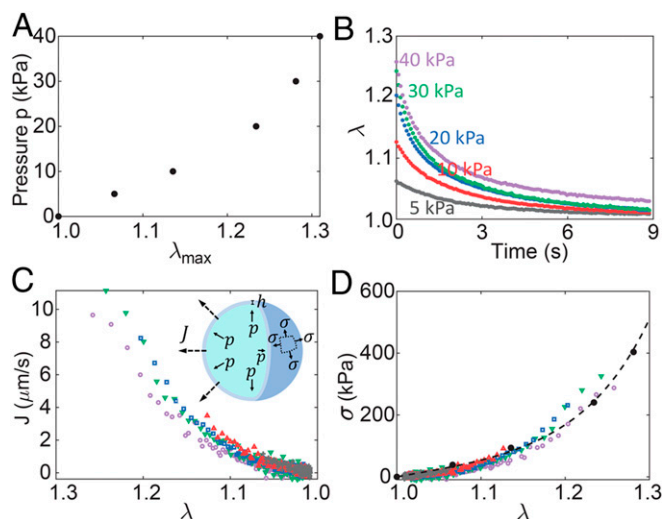https://doi.org/10.1073/pnas.2022422118

Fig. 3. Mechanical and kinetic properties of BM determined from experimental results. (*A*) The stretch of the membrane at steady state (maximum stretch) for different injection pressure. (*B*) Deflation curves in term of radial expansion $\lambda = r/R_0$ at varying injection pressure. (*C*) Fluid flux of BM as a function of the stretch of the membrane. During the deflation, fluid flux $J = dr/dt$. Insert, schematics of BM: inner fluid pressure, p; biaxial stress on spherical membrane, σ; fluid flux, J. (*D*) Constitutive behavior of the BM obtained from (*A*) by using $R_0 = 32.5\mu m$ and $H = 2.5\mu m$. The dashed curve is the fitting result from Fung's model. Using Darcy's law, we can convert the fluid flux curve in *C* to the constitutive relation of the BM with the fitted permeability of the membrane $k = 6.95 \times 10^{-19}$ m^2.

we can obtain the stress–strain relationship of the BM under uniaxial tension as $\sigma = G(\lambda^2 - \lambda^{-1})e^{b(\lambda^2 + 2\lambda^{-1} - 3)}$. Using the measured material parameters, we further plot both uniaxial and equal-biaxial tangent modulus of the BM (defined as $K = d\sigma/d\varepsilon$ with σ representing the true stress and $\varepsilon = ln\lambda$ representing the true strain for either uniaxial or equal-biaxial deformation) as a function of strain in Fig. 4*A*. With a slight increase of strain, the tangent modulus K of BM increases by several times for both uniaxial and biaxial deformation. This is in direct contrast to the wide linear elastic regime observed on reconstituted Matrigel (24, 25), indicating distinct structural characteristics between natural BMs and Matrigel reconstituted from BM extracts. Indeed, clear fibrous network structures can be observed in the intact BMs, as shown by the TEM images in Fig. 1*C*. These fibrous networks of biopolymers are known to cause a strong, nonlinear stiffening effect (26), due to various mechanisms including entropic elasticity of individual filaments, geometric

effects due to fiber bending and buckling, and collective network effects governed by critical phenomena (27–33).

Strain stiffening of soft biological tissues has been widely observed and known to play important yet different roles in various biological processes (24, 34, 35). Herein, we discuss the possible effect of the strain stiffening of BMs on their functions. It has been well known that a hyperelastic balloon under inflation often suffers from snap-through instability when the internal pressure or the radial expansion is beyond a critical value (36–38). Fig. 4*B* plots the relationship between the inflating pressure and the radial expansion of a balloon made up of a neo-Hookean membrane (such as a latex membrane). The relationship between the internal pressure and the radial expansion of the balloon is nonmonotonic, and there is a peak pressure with a corresponding critical radial expansion: λ=1.38. As a result, when the radial expansion ratio reaches the critical value, the balloon can dramatically increase its size without requiring a further increase of the pressure, as shown by the horizontal line in Fig. 4*B*. For a latex balloon, such drastic expansion during the snap-through process often leads to rupture. More interestingly, if the volume of the balloon is controlled to increase gradually, the internal pressure drops with the further increase of the volume after the balloon expansion exceeds the critical value. If the mechanical behavior of the BM is similar to that of a latex balloon, after the radial expansion of the BM exceeds 1.38, further growth of tissue inside (such as a tumor) reduces mechanical constraint from the BM, which may lead to irregular tissue morphology or rapid tumor expansion (39).

It is worth noting that the nonmonotonic relationship between the inflating pressure and radial expansion of a hyperelastic balloon (and the resulting snap-through instability) is not a consequence of special mechanical properties of the material. Instead, it is due to the significant reduction of the balloon thickness with its radial expansion. So, the descending part of the pressure versus the radial expansion curve (for a neo-Hookean elastomeric balloon) in Fig. 4*B* can be referred to as geometrical softening. One way to avert such snap-through instability is to introduce significant strain stiffening in the material at relatively small deformation (with biaxial stretch smaller than the critical stretch: 1.38) to compensate the geometrical softening effect. As shown in Fig. 4*A*, the BM indeed exhibits a strong strain-stiffening effect starting at a small deformation. As a result, the relationship between the inflating pressure and the radial expansion of the BM is monotonic, and snap-through instability does not occur, as shown in Figs. 3*A* and 4*B*. These results indicate the importance of the nonlinear elasticity of BMs in maintaining tissue mechanical integrity during growth and development. In the following, we will further elaborate the necessary strain stiffening of the material for preventing snap-through instability of the balloon.
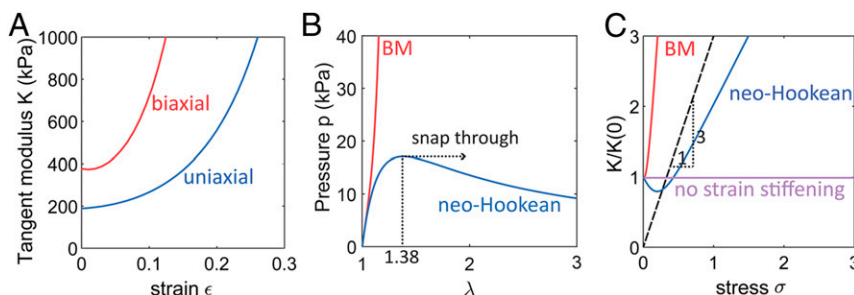

Fig. 4. Nonlinear elastic behavior of BMs. (*A*) Tangent modulus of BMs (defined in the text) as a function of true strain for equal-biaxial tension and uniaxial tension. (*B*) The relationship between the inflating pressure as a function of radial expansion of a balloon made up of a neo-Hookean material compared to that of BMs. (*C*) If the strain-stiffening curve of the material such as BM does not intersect the dashed line ($K = 3\sigma$), snap-through instability can be avoided. If the strain-stiffening curve of the material, such as neo-Hookean material or linear elastic material, intersect with the dashed line, snap-through instability of the balloon can occur. It is noted that in *C*, both of the tangent modulus and stress are normalized by the tangent modulus of the material in free-standing state.

To avoid the snap-through or structural softening of a balloon, the relationship between the internal pressure and its radial expansion needs to be monotonic, namely $dp/d\lambda > 0$. With the material incompressibility and force balance, we can show that the condition above is equivalent to $K > 3\sigma$, where K is biaxial tangent modulus defined above and σ is the true equal-biaxial stress. In Fig. 4*C*, $K = 3\sigma$ is shown by the dashed line. We can also plot biaxial tangent modulus as a function of the true biaxial stress for different hyperelastic material models in Fig. 4*C*. For a hyperelastic material whose strain stiffening is significant enough like the BM, its strain-stiffening curve does not intersect the dashed line ($K = 3\sigma$), as shown in Fig. 4*C*; therefore, snap-through instability or structural softening can be prevented. In contrast, if the strain-stiffening curve intersects the dashed line (e.g., for neo-Hookean material marked or materials with no strain-stiffening effect), snap-through instability or structural softening occurs. It is noted that using the fitted parameters of the BM as shown above, we predict the mechanical behavior of the BM with the deformation much larger than the one shown in the experiment, which may be beyond the rupturing point of the BM.

Discussion

In this work, we introduce a facile method based on inflation–deflation experiments to in situ measure the mechanics of BM in breast cancer spheroid. We find that BMs can be well captured as a permeable hyperelastic material. As the inflation pressure is released, the inflated BM fully returns to its initial state; this outstanding elastic property may provide mechanical protection to its internal structures. Moreover, the inflation–deflation method we introduce here explores the global mechanics of BMs, in contrast to other local measurements on fragmented BM such as AFM. Two critical mechanical properties, elastic modulus and permeability, can be directly determined from the deflation process independent of specific material models. We believe this is an important advantage of the current inflation–deflation method compared with other methods such as indentation test. For an indentation test, a specific constitutive model for the BM has to be assumed in the first place to enable the conversion of the experimental measurements (e.g., indentation force versus indentation depth) to the stress–strain relationship of a BM. Justifying an appropriate selection of the constitutive model can be very challenging given the highly nonlinear elastic behavior and the poroelastic nature of BMs. Consequently, such justification is often missing or inadequate in the previous studies. Thus, the inflation–deflation method developed in the current work may be used to measure mechanics of intact BMs in different systems and during both healthy and disease states.

Furthermore, our in situ measurement reveals marked nonlinear elasticity of the BMs whose onset is below 10% of strain. This behavior is in direct contrast to the large linear elastic regime observed in reconstituted Matrigel (24, 25) yet is consistent with a wide variety of biological tissues and biopolymer networks (26, 40, 41). This nonlinear stiffening behavior of the BM may have an important role in maintaining tissue mechanical integrity during growth and deformation (e.g., to avoid structural instability), which is a classical behavior leading to drastic expansion or even rupture when inflating most elastomeric balloons.

Materials and Methods

Cancer Spheroid Culture and Isolation. The human breast cancer MDA-MB-231 cells (ATCC) are cultured in Dulbecco's Modified Eagle Medium (Gibco) with 10% fetal bovine serum (Gibco) and 1% penicillin–streptomycin (Gibco) at 37 °C with 5% CO_2. The individual cells at the log phase are seeded onto the gelled Matrigel bed (10 mg/mL, Corning, 354234) and are cultured to allow proliferation for 5 d to form clusters. Culture medium supplemented with 0.2 mg/mL Matrigel is replaced every 2 d. BM is secreted and generated by cells during the growth of these multicellular cancer spheroids.

To isolate these cancer spheroids, samples are placed in ice-cold PBS to break down the Matrigel, and then centrifuged at 100 g to remove the supernatant Matrigel fragments. The intact cancer spheroids out of Matrigel are collected by resuspending them in PBS and are then seeded on a glass-bottom Petri-dish for immunofluorescence staining or microinjection experiments.

Immunofluorescence Staining. The isolated cancer spheroids are firstly fixed with 4% paraformaldehyde at room temperature for 30 min. Then, the spheroids are permeabilized with 0.2% Triton X-100 in PBS for 15 min. After that, the samples are blocked with 5% bovine serum albumin (BSA) in PBS for 1 h at room temperature and subsequently incubated with the primary antibody for laminin-5 (1:100 in PBS with 0.1% BSA, Santa Cruz Biotechnology, sc-13578) overnight at 4 °C. The samples are then incubated with the second antibody Alexa-488 goat anti-mouse (1:300, Thermo Fisher, A-11001) for 1 h at room temperature in darkness. The nuclei are stained with Hoechst 33342 (Sigma, 14533) before imaged under a confocal microscopy (Leica SP8).

Microinjection. The FemtoJet microjector (5248, Eppendorf) is mounted on a confocal microcopy (Lecia TCL SP8) equipped with a 25× water-immersed objective (0.9 numerical aperture) and a cage incubator (37 °C, Okolab). A glass-made microneedle (2 μm in diameter, Eppendorf) is loaded with PBS buffer. Then it is manipulated to penetrate the surrounding BM, placing the needle tip inside the spheroid. To perform an inflation–deflation cycle, the injection pressure and its duration are predefined in the microinjector connecting to the microneedle. After manually starting the injection protocol, the BM would quickly inflate to a steady state, and then gradually deflate back to its initial size. Under each pressure, two or more inflation–deflation cycles are performed for one sample. Bright-field imaging at 14 Hz is applied to record the shape and size of a BM. From the recorded movies, the radius of BMs is determined by using a customized algorithm in MATALB.

Electron Microscopy. The sample preparation follows a previously established protocol (20). Briefly, the cancer spheroids cultured on a Matrigel bed are fixed with 2.5% glutaraldehyde in 0.1 M sodium cacodylate for 1 h. Then, samples are postfixed by 1% osmium tetroxide in 0.1 M sodium cacodylate at 4 °C for 30 min and dehydrated in graded ethanol. After that, the samples are embedded in epoxy resin, followed by sectioning. Only cross-sections of the spheroid above the Matrigel surface are collected and stained with 1.4% uranyl acetate and then with lead citrate. Sections are imaged with a Hitachi H-7650. The BM thicknesses are measured from the TEM images by using ImageJ.

Data Availability. All study data are included in the article and/or supporting information.

1. P. D. Yurchenco, Basement membranes: Cell scaffoldings and signaling platforms. *Cold Spring Harb. Perspect. Biol.* **3**, a004911 (2011).
2. A. Glentis, V. Gurchenkov, D. Matic Vignjevic, Assembly, heterogeneity, and breaching of the basement membranes. *Cell Adhes. Migr.* **8**, 236–245 (2014).
3. F. T. Bosman, M. Havenith, J. P. M. Cleutjens, Basement membranes in cancer. *Ultrastruct. Pathol.* **8**, 291–304 (1985).
4. A. W. Lambert, D. R. Pattabiraman, R. A. Weinberg, Emerging biological principles of metastasis. *Cell* **168**, 670–691 (2017).
5. P. N. Furness, E. W. Lam, Patterns of basement membrane deposition in benign, premalignant, and malignant endometrium. *J. Clin. Pathol.* **40**, 1320–1323 (1987).
6. J. Chang, O. Chaudhuri, Beyond proteases: Basement membrane mechanics and cancer invasion. *J. Cell Biol.* **218**, 2456–2469 (2019).
7. R. Reuten et al., Basement membrane stiffness determines metastases formation. *Nat. Mater.* 10.1038/s41563-020-00894-0 (2021).
8. J. P. Caulfield, M. G. Farquhar, The permeability of glomerular capillaries to graded dextrans. Identification of the basement membrane as the primary filtration barrier. *J. Cell Biol.* **63**, 883–903 (1974).
9. J. C. Serrano, S. K. Gupta, R. D. Kamm, M. Guo, In pursuit of designing multicellular engineered living systems: A fluid mechanical perspective. *Annu. Rev. Fluid Mech.* **53**, 411–437 (2021).
10. J. Candiello et al., Biomechanical properties of native basement membranes. *FEBS J.* **274**, 2897–2908 (2007).

Li et al.
Nonlinear elasticity of biological basement membrane revealed by rapid inflation and deflation

PNAS | 5 of 6
https://doi.org/10.1073/pnas.2022422118

11. J. A. Last, S. J. Liliensiek, P. F. Nealey, C. J. Murphy, Determining the mechanical properties of human corneal basement membranes with atomic force microscopy. *J. Struct. Biol.* **167**, 19–24 (2009).

12. J. Crest, A. Diz-Muñoz, D. Y. Chen, D. A. Fletcher, D. Bilder, Organ sculpting by patterned extracellular matrix stiffness. *eLife* **6**, e24958 (2017).

13. G. Fabris *et al.*, Nanoscale topography and poroelastic properties of model tissue breast gland basement membranes. *Biophys. J.* **115**, 1770–1782 (2018).

14. A. M. Howard *et al.*, DSS-induced damage to basement membranes is repaired by matrix replacement and crosslinking. *J. Cell Sci.* **132**, jcs226860 (2019).

15. V. F. Fiore *et al.*, Mechanics of a multilayer epithelium instruct tumour architecture and function. *Nature* **585**, 433–439 (2020).

16. G. Bhave, S. Colon, N. Ferrell, The sulfilimine cross-link of collagen IV contributes to kidney tubular basement membrane stiffness. *Am. J. Physiol. Renal Physiol.* **313**, F596–F602 (2017).

17. A. Glentis *et al.*, Cancer-associated fibroblasts induce metalloprotease-independent cancer cell invasion of the basement membrane. *Nat. Commun.* **8**, 924 (2017).

18. J. Debnath, S. K. Muthuswamy, J. S. Brugge, Morphogenesis and oncogenesis of MCF-10A mammary epithelial acini grown in three-dimensional basement membrane cultures. *Methods* **30**, 256–268 (2003).

19. Y. L. Han *et al.*, Cell swelling, softening and invasion in a three-dimensional breast cancer model. *Nat. Phys.* **16**, 101–108 (2020).

20. J. M. Underwood *et al.*, The ultrastructure of MCF-10A acini. *J. Cell. Physiol.* **208**, 141–148 (2006).

21. Y.-c. Fung, *Biomechanics: Mechanical Properties of Living Tissues* (Springer Science & Business Media, 2013).

22. N. Ferrell *et al.*, Effects of pressure and electrical charge on macromolecular transport across bovine lens basement membrane. *Biophys. J.* **104**, 1476–1484 (2013).

23. G. A. Abrams, S. L. Goodman, P. F. Nealey, M. Franco, C. J. Murphy, Nanoscale topography of the basement membrane underlying the corneal epithelium of the rhesus macaque. *Cell Tissue Res.* **299**, 39–46 (2000).

24. Y. L. Han *et al.*, Cell contraction induces long-ranged stress stiffening in the extracellular matrix. *Proc. Natl. Acad. Sci. U.S.A.* **115**, 4075–4080 (2018).

25. M. Rausch *et al.*, Measurement of skeletal muscle fiber contractility with high-speed traction microscopy. *Biophys. J.* **118**, 657–666 (2020).

26. C. Storm, J. J. Pastore, F. C. MacKintosh, T. C. Lubensky, P. A. Janmey, Nonlinear elasticity in biological gels. *Nature* **435**, 191–194 (2005).

27. O. Lieleg, M. M. Claessens, C. Heussinger, E. Frey, A. R. Bausch, Mechanics of bundled semiflexible polymer networks. *Phys. Rev. Lett.* **99**, 088102 (2007).

28. M. L. Gardel *et al.*, Elastic behavior of cross-linked and bundled actin networks. *Science* **304**, 1301–1305 (2004).

29. C. P. Broedersz, M. Sheinman, F. C. Mackintosh, Filament-length-controlled elasticity in 3D fiber networks. *Phys. Rev. Lett.* **108**, 078102 (2012).

30. C. P. Broedersz, F. C. MacKintosh, Modeling semiflexible polymer networks. *Rev. Mod. Phys.* **86**, 995 (2014).

31. P. R. Onck, T. Koeman, T. van Dillen, E. van der Giessen, Alternative explanation of stiffening in cross-linked semiflexible networks. *Phys. Rev. Lett.* **95**, 178102 (2005).

32. M. Wyart, H. Liang, A. Kabla, L. Mahadevan, Elasticity of floppy and stiff random networks. *Phys. Rev. Lett.* **101**, 215501 (2008).

33. A. Sharma *et al.*, Strain-controlled criticality governs the nonlinear mechanics of fibre networks. *Nat. Phys.* **12**, 584–587 (2016).

34. S. van Helvert, P. Friedl, Strain stiffening of fibrillar collagen during individual and collective cell migration identified by AFM nanoindentation. *ACS Appl. Mater. Interfaces* **8**, 21946–21955 (2016).

35. J. Hu *et al.*, High stretchability, strength, and toughness of living cells enabled by hyperelastic vimentin intermediate filaments. *Proc. Natl. Acad. Sci. U.S.A.* **116**, 17175–17180 (2019).

36. I. Müller, H. Struchtrup, Inflating a rubber balloon. *Math. Mech. Solids* **7**, 569–577 (2002).

37. A. Needleman, Inflation of spherical rubber balloons. *Int. J. Solids Struct.* **13**, 409–421 (1977).

38. H. Alexander, Tensile instability of initially spherical balloons. *Int. J. Eng. Sci.* **9**, 151–160 (1971).

39. D. K. Bogen, T. A. McMahon, Do cardiac aneurysms blow out? *Biophys. J.* **27**, 301–316 (1979).

40. W. Yang *et al.*, On the tear resistance of skin. *Nat. Commun.* **6**, 6649 (2015).

41. J. Wu *et al.*, Natural hydrogel in American lobster: A soft armor with high toughness and strength. *Acta Biomater.* **88**, 102–110 (2019).